

Operational measurement of relativistic equilibrium from stochastic fields alone

Ira Wolfson*

*Department of Electrical and Electronic Engineering,
Braude Academic College of Engineering, Karmiel, Israel*

(Dated: March 23, 2026)

The inverse-temperature four-vector $\beta^\mu = u^\mu/(k_B T_0)$ has been the theoretically accepted description of relativistic equilibrium since the work of van Kampen and Israel, yet no experiment has ever reconstructed β^μ as a single observable. All existing methods—Thomson scattering, spectral fitting, blast-wave models—infer rest-frame temperature and flow velocity from separate measurements and model-dependent assumptions. We propose the first protocol that extracts both components of β^μ from the *same* passive observable: electromagnetic fluctuation correlations emitted by a drifting medium. A dimensionless E – B cross-spectral ratio yields the drift velocity directly from the Lorentz mixing of the field-strength tensor, while angle-resolved noise power governed by the covariant fluctuation–dissipation theorem provides the rest-frame temperature through a ratio method that cancels absolute amplitude. Together, these observables reconstruct β^μ without external probes, spectral lines, or absolute radiometric calibration. The protocol also enables the first direct experimental test of whether the thermal state of a relativistic medium transforms as a four-vector under Lorentz boosts—a question that has remained purely theoretical since the Planck–Ott–Landsberg controversy began in 1907. Such a verified baseline is a prerequisite for assessing temperature measurements in systems where β^μ cannot be independently checked: in relativistic heavy-ion collisions, the four-vector transformation is assumed but never tested; in astrophysical sources such as gamma-ray bursts, the principle of extracting thermal parameters from passive fluctuation statistics could inform single-sightline analyses once the multi-angle protocol has been validated. Monte Carlo simulations parameterized to the HIGGINS dual 100 TW laser-plasma facility demonstrate sub-percent rest-frame temperature recovery for Lorentz factors $\gamma = 1.05$ – 10 , with robustness to additive noise at signal-to-noise ratios $\gtrsim 10$. The method requires relative channel calibration, knowledge of the medium response function, and local thermodynamic equilibrium, but eliminates the need for absolutely calibrated radiometers, active probes, or spectral line identification.

I. INTRODUCTION

Relativistic thermodynamic equilibrium is described not by a scalar temperature but by the inverse-temperature four-vector $\beta^\mu = u^\mu/(k_B T_0)$ [1, 2]. This covariant structure, originating in the nonequilibrium statistical operator formalism of Zubarev [3] and placed on rigorous footing by van Kampen [4] and Israel [5], now underpins relativistic dissipative hydrodynamics and the Kubo–Martin–Schwinger condition in thermal field theory [6–8]. Despite this theoretical consensus, β^μ has never been reconstructed as a unified quantity from a single experimental measurement. All current techniques infer the rest-frame temperature T_0 and the four-velocity u^μ from independent observables, and each approach carries structural limitations that prevent model-independent access to the covariant thermal state:

- *Thomson scattering* [9] provides high-accuracy electron temperature measurements but requires an external laser probe and determines the flow velocity from an independent Doppler shift measurement. Temperature and velocity are separate observables, obtained from different physical mechanisms, assembled into β^μ only after the fact.

- *Spectral radiometry* [10, 11] infers temperature by fitting thermal emission spectra, requiring absolutely calibrated detectors and knowledge of the emission mechanism. Drift velocity must be supplied independently, typically from Doppler-shifted spectral lines.
- *Heavy-ion methods* (blast-wave fits [12], thermal dilepton spectra) extract temperature from invariant-mass distributions and velocity from collective flow observables (v_1 , v_2), but both require extensive modeling of freeze-out geometry, equation of state, and non-equilibrium evolution. The resulting β^μ is a fit parameter of a hydrodynamic model, not a direct observable.
- *Astrophysical observations* [13] of relativistic jets and fireballs provide single-line-of-sight data only, making the angle-resolved measurement required to reconstruct a four-vector geometrically impossible. Cosmological and gravitational redshifts are degenerate with thermal Doppler shifts, preventing model-independent separation of T_0 and β .

A deeper consequence of this observational gap is that the century-old question of how thermodynamic quantities transform under Lorentz boosts has never been directly tested. The Planck–Ott–Landsberg controversy [14–16]—whether a moving body appears hotter, cooler, or unchanged—was resolved theoretically by

* wolfsoni@braude.ac.il

recognizing that temperature is not a scalar but a component of β^μ [1, 4, 5]. But this resolution rests entirely on theoretical arguments and thermodynamic consistency; no experiment has ever measured the thermal state of a relativistic medium at multiple observation angles and verified that the results are consistent with four-vector transformation. (Angle-resolved synchrotron radiation from storage rings, while relativistic and well-characterized, is coherent emission from individual accelerating charges, not equilibrium thermal fluctuations; it tests classical electrodynamics of single particles, not statistical-mechanical properties of a thermal ensemble.) A protocol that reconstructs β^μ from angular measurements would simultaneously serve as the first direct empirical test of this covariant structure.

The implications extend beyond the laboratory. In relativistic heavy-ion collisions, temperature and flow velocity are extracted from particle spectra under the assumption that the thermal state transforms as β^μ —but this assumption is built into the hydrodynamic analysis framework, not tested by it. A controlled laboratory measurement that confirms (or falsifies) the four-vector transformation law provides the empirical baseline against which heavy-ion thermal analyses can be critically assessed. Similarly, in astrophysical settings such as gamma-ray bursts, the principle of thermal-state reconstruction from passive fluctuation statistics could inform single-sightline spectral analyses, though adapting the multi-angle protocol to single-line-of-sight data would require further theoretical development. The laboratory measurement is therefore not a proof of concept for its own sake: it is the necessary first step in a chain that extends from plasma diagnostics to high-energy nuclear physics and relativistic astrophysics.

Passive thermal noise has been used to infer bulk drift velocity in nonrelativistic space plasmas via quasi-thermal noise spectroscopy [17], and full electromagnetic fluctuation tensors for drifting relativistic plasmas have been computed from kinetic theory [18], but no prior work has exploited E – B cross-correlations or formulated an operational reconstruction of β^μ from stochastic field statistics.

We show that passive electromagnetic fluctuations emitted by a drifting thermal medium encode both components of β^μ in their correlation structure. Two observables, extracted from the same stochastic field ensemble, provide this information: (i) the dimensionless cross-spectral ratio $R = \langle \delta E'_y \delta B'_x \rangle / \langle |\delta E'_y|^2 \rangle$, which yields the drift velocity from the Lorentz mixing of the field-strength tensor without any intensity calibration; and (ii) angle-resolved noise spectra governed by the covariant fluctuation–dissipation theorem, from which the rest-frame temperature is recovered via a ratio method that cancels absolute amplitude. The E – B cross-correlation is a genuinely new observable with no counterpart in conventional radiometry, Stokes polarimetry, or Thomson diagnostics.

The relationship to existing physics is analogous to

that of Johnson–Nyquist noise thermometry [19, 20] to Planck’s radiation law: the underlying thermal physics—Planck’s spectrum—was already understood, but the operational protocol of measuring voltage noise across a resistor rather than spectral radiance from a cavity constituted a distinct and practically important diagnostic [21]. Here, the covariant fluctuation–dissipation theorem is well established; the contribution is the identification of observables and a complete measurement protocol that provides operational access to β^μ for the first time.

We characterize the statistical precision and noise robustness of this protocol using Monte Carlo simulations parameterized to the HIGGINS dual 100 TW laser-plasma facility at the Weizmann Institute of Science [22].

II. VELOCITY EXTRACTION FROM FLUCTUATION CROSS-CORRELATIONS

We begin from the electromagnetic field-strength tensor

$$F^{\mu\rho} = \begin{pmatrix} 0 & -E_x & -E_y & -E_z \\ E_x & 0 & -B_z & B_y \\ E_y & B_z & 0 & -B_x \\ E_z & -B_y & B_x & 0 \end{pmatrix}, \quad (1)$$

Under a Lorentz boost with velocity $v = \beta c$ along \hat{z} , the field tensor transforms as $F'^{\mu\rho} = \Lambda^\mu_\alpha \Lambda^\rho_\beta F^{\alpha\beta}$, where

$$\Lambda^\mu_\rho = \begin{pmatrix} \gamma & 0 & 0 & -\gamma\beta \\ 0 & 1 & 0 & 0 \\ 0 & 0 & 1 & 0 \\ -\gamma\beta & 0 & 0 & \gamma \end{pmatrix}. \quad (2)$$

The transverse components of the boosted tensor mix electric and magnetic fields:

$$F'^{02} = \gamma(F^{02} + \beta F^{32}) = -\gamma(E_y + vB_x), \quad (3)$$

$$F'^{13} = \gamma(F^{13} + \beta F^{10}) = -\gamma\left(B_x + \frac{v}{c^2}E_y\right), \quad (4)$$

which yield the standard field transformations

$$E'_y = \gamma(E_y + vB_x), \quad (5)$$

$$B'_x = \gamma\left(B_x + \frac{v}{c^2}E_y\right). \quad (6)$$

Equations (5)–(6) are the key observation: the boost mixes the (E_y, B_x) sector of $F^{\mu\rho}$, so that even if E_y and B_x are uncorrelated in the rest frame, their laboratory-frame counterparts E'_y and B'_x acquire a cross-correlation proportional to v .

In the rest frame of an isotropic equilibrium medium, electric and magnetic fluctuations are uncorrelated:

$$\langle \delta E_y \delta B_x \rangle = 0. \quad (7)$$

Computing the laboratory-frame cross-spectral density from Eqs. (5)–(6) and using Eq. (7):

$$\langle \delta E'_y \delta B'^*_x \rangle = \gamma^2 \left[v \langle |B_x|^2 \rangle + \frac{v}{c^2} \langle |E_y|^2 \rangle \right]. \quad (8)$$

The experiment detects the radiated noise in the far field outside the medium, where the radiation propagates through vacuum. This is a design requirement, not an approximation: by placing the detector array outside the plasma boundary, the vacuum E – B relation holds by construction, and no in-medium refractive corrections enter the velocity extraction. Over a full oscillation period the Poynting vector exchanges energy equally between the electric and magnetic fields, giving a time-averaged flux $\langle S \rangle = |E|^2/(2Z) = |H|^2 Z/2$, where Z is the wave impedance of the medium. In vacuum $Z = Z_0 = \mu_0 c$ and $B = \mu_0 H$, so

$$\langle |E|^2 \rangle = c^2 \langle |B|^2 \rangle. \quad (9)$$

Substituting Eq. (9) into Eq. (8) and normalizing by the auto-spectral density $\langle |\delta E'_y|^2 \rangle$ yields the dimensionless ratio

$$R \equiv \frac{\langle \delta E'_y \delta B'_x \rangle}{\langle |\delta E'_y|^2 \rangle} = \frac{2\beta}{1 + \beta^2}. \quad (10)$$

To see this, note that the denominator follows from Eq. (5): $\langle |\delta E'_y|^2 \rangle = \gamma^2 [\langle |E_y|^2 \rangle + \beta^2 \langle |B_x|^2 \rangle] = \gamma^2 (1 + \beta^2) \langle |E_y|^2 \rangle$, where the second equality uses the vacuum relation Eq. (9). Similarly, the numerator is $\gamma^2 \cdot 2\beta \langle |E_y|^2 \rangle$ from Eq. (8); the ratio gives $2\beta/(1 + \beta^2)$. This is analytically invertible:

$$\beta = \frac{1 - \sqrt{1 - R^2}}{R}, \quad (11)$$

providing a direct kinematic observable from passive field correlations alone. The ratio is dimensionless and independent of detector gain or absolute calibration, provided the relative transfer functions of the electric and magnetic channels are stable or known.

A detector placed inside a dispersive medium with impedance $Z(\omega) = Z_0/n(\omega)$ would observe a modified E – B ratio; the vacuum condition Eq. (9) is replaced by $\langle |E|^2 \rangle = (c/n)^2 \langle |B|^2 \rangle$. This introduces medium-dependent calibration factors but does not alter the reconstruction principle.

Crucially, Eq. (10) relies only on the isotropy of the rest-frame fluctuations and the structure of the Lorentz group acting on $F^{\mu\rho}$, not on thermal equilibrium per se; it therefore remains valid for any medium whose rest-frame noise is isotropic, even if the distribution deviates from the Jüttner form [6, 23].

III. TEMPERATURE RECONSTRUCTION FROM ANGLE-RESOLVED NOISE SPECTRA

A. Covariant fluctuation–dissipation theorem

The electromagnetic response of a linear medium is encoded in the retarded photon self-energy $\Pi_R^{\mu\rho}(p)$, which determines how the medium polarizes in response to an

applied field. The fluctuation properties of the medium are encoded in the symmetrized self-energy $\Pi_S^{\mu\rho}(p) = \frac{1}{2} \langle \{j^\mu(p), j^\rho(-p)\} \rangle$, which is the Fourier transform of the symmetrized current–current correlator. In thermal equilibrium, these two tensors are not independent; the covariant fluctuation–dissipation theorem relates them as [7, 8, 21]

$$\Pi_S^{\mu\rho}(p) = \coth \frac{\beta \cdot p}{2} 2 \text{Im} \Pi_R^{\mu\rho}(p), \quad (12)$$

where $\beta \cdot p = \beta^\mu p_\mu$ is the Lorentz-invariant contraction of the inverse-temperature four-vector with the photon four-momentum. The \coth factor encodes the thermal occupation of field modes; it reduces to the Bose–Einstein distribution plus vacuum contribution. This formulation assumes that the medium is in global or local thermodynamic equilibrium in its comoving frame.

To connect Eq. (12) to a measurable quantity, we project onto the electric field. The electric-field power spectral density (PSD) at laboratory frequency ω' and observation angle θ is

$$S_E(\omega', \theta) \equiv \int dt e^{i\omega' t} \langle \delta E'_\perp(\mathbf{x}, t) \delta E'_\perp(\mathbf{x}, 0) \rangle_\theta. \quad (13)$$

The current fluctuations $\Pi_S^{\mu\rho}$ source electric-field fluctuations through Maxwell's equations; for the transverse electric component the relevant projection gives $S_E \propto \omega^2 \Pi_S^{ii}/|\epsilon(\omega)|^2$, where $\epsilon(\omega)$ is the dielectric function. In the rest frame, the dissipative part of the response is related to the conductivity by $\text{Im} \Pi_R^{ii}(\omega) \propto \omega \sigma(\omega)$, where $\sigma(\omega)$ is the real part of the frequency-dependent conductivity. Combining these relations with Eq. (12) yields the rest-frame PSD:

$$S_E^{(\text{rest})}(\omega) \propto \coth \left(\frac{\hbar\omega}{2k_B T_0} \right) \omega \sigma(\omega), \quad (14)$$

where the proportionality absorbs the factor $\omega^2/|\epsilon(\omega)|^2$ from the projection step as well as numerical constants. We will need to restore the explicit ω -dependence of these prefactors when transforming between frames.

B. Classical limit and laboratory-frame PSD

In the classical regime $\hbar\omega \ll k_B T_0$, $\coth(\hbar\omega/2k_B T_0) \rightarrow 2k_B T_0/\hbar\omega$ and the rest-frame PSD reduces to $S_E^{(\text{rest})}(\omega) \propto T_0 \sigma(\omega)$, up to frequency-dependent prefactors that cancel in ratio observables. For the HIGGINS parameters used below, $k_B T_0/\hbar\omega_p = 8512$, so the classical approximation holds to better than 10^{-4} across the entire frequency window. More generally, the method applies whenever $k_B T_0 \gg \hbar\omega_{\text{max}}$, i.e., at temperatures well above the quantum scale set by the highest detected frequency.

Consider a medium in global equilibrium drifting at velocity $v = \beta c$ relative to the laboratory. Define the

observation angle θ and Doppler factor D by

$$\cos \theta = \hat{k}' \cdot \hat{\beta}, \quad D \equiv \gamma(1 - \beta \cos \theta), \quad (15)$$

so that the rest-frame and laboratory frequencies are related by $\omega = D\omega'$. The transformation of the PSD between frames involves the Lorentz invariance of I_ν/ν^3 (relativistic beaming) combined with the frequency-dependent density-of-states prefactor in the projection from $\Pi_S^{\mu\rho}$ to the electric-field PSD. The full derivation, which tracks all powers of D explicitly, is given in Appendix A. The result is the laboratory-frame PSD [7, 11, 24]:

$$S(\omega', \theta) \propto \frac{T_0}{D} \sigma(D\omega') = \frac{T_0}{\gamma(1 - \beta \cos \theta)} \sigma(\gamma\omega'(1 - \beta \cos \theta)). \quad (16)$$

This is the central observable for temperature reconstruction. The prefactor T_0/D is the angle-dependent effective temperature seen by a laboratory detector; the argument of σ is the Doppler-shifted rest-frame frequency $\omega = D\omega'$, not the laboratory frequency ω' .

IV. RELATIONSHIP TO THERMAL EMISSION AND KIRCHHOFF'S LAW

A natural question is whether the proposed method reduces to measuring Doppler-shifted thermal emission, a well-understood phenomenon. The answer is yes in terms of underlying physics, and no in terms of observables and calibration requirements.

The connection to thermal emission is exact and foundational. In equilibrium, Kirchhoff's law relates spontaneous emission to absorption [11]:

$$j_\nu = \alpha_\nu B_\nu(T), \quad (17)$$

where j_ν is the emission coefficient, α_ν the absorption coefficient, and B_ν the Planck function. In the classical limit and for optically thin emission, the Lorentz transformation of specific intensity ($I'_\nu/\nu'^3 = I_\nu/\nu^3$) implies that radiation observed at laboratory angle θ from a drifting source acquires the same angular factor $T_0/[\gamma(1 - \beta \cos \theta)]$ that appears in Eq. (16) [11].

This equivalence is not a weakness of the proposal; it is its physical basis. The relationship is precisely analogous to that between Johnson–Nyquist noise thermometry and Planck's radiation law. Johnson–Nyquist noise is thermal electromagnetic radiation confined to a circuit, and the fluctuation–dissipation theorem and Kirchhoff's law are equivalent formulations of equilibrium fluctuation physics [21, 25]. Johnson's 1928 experiment [19] did not cease to be novel because Planck's law was already known. What was novel was the *operational protocol*: measuring voltage noise across a resistor to determine temperature, rather than measuring spectral radiance from a cavity. The observable (voltage variance), the required calibration (resistance, not absolute radiometric standards), and the practical advantages (broadband,

compact, no optical path) were all distinct from radiometry, despite the shared underlying physics.

The present proposal stands in the same relationship to boosted thermal radiation. Three specific differences distinguish it from conventional radiometric thermometry:

(i) *Different observable.* The E – B cross-correlation ratio $R = \langle \delta E'_y \delta B'_x \rangle / \langle |\delta E'_y|^2 \rangle$ exploits the off-diagonal sector of the boosted field-strength tensor $F^{\mu\rho}$. Standard radiometry and Stokes polarimetry measure intensity correlations within the electric field alone ($\langle E_i E_j^* \rangle$); they do not access the E – B cross-spectral density that encodes the velocity.

(ii) *Different calibration requirements.* The velocity extraction requires no absolute calibration whatsoever—only stability of the relative E/B channel gain. The temperature extraction uses a ratio of boosted to rest-frame power that cancels absolute amplitude factors. By contrast, radiometric temperature measurement requires absolutely calibrated detectors or reference sources.

(iii) *Simultaneous β and T_0 from a single measurement.* Conventional radiometry of a moving source yields $T_{\text{eff}}(\theta) = T_0/D(\theta)$, but cannot disentangle T_0 from β without independent velocity information. The E – B ratio provides this velocity from the same field measurement, closing the system.

V. COMPARISON WITH EXISTING DIAGNOSTICS

Conventional radiometry relies on absolute intensity or spectral features [10], and active techniques such as Thomson scattering extract temperature and velocity from calibrated spectral fits [9]. The present method instead exploits field correlations and the angular structure of stochastic radiation. Table I summarizes the key differences.

The E – B cross-correlation observable (Eq. 10) accesses a sector of the field-strength tensor not probed by standard techniques. Unlike Stokes-parameter polarimetry [11], which characterizes intensity correlations within the electric field alone ($\langle E_i E_j^* \rangle$), the present observable involves cross-correlations between electric and magnetic fields ($\langle E_i B_j^* \rangle$). This coupling arises from Lorentz mixing of field components and directly encodes the bulk velocity, providing kinematic information not contained in polarization measurements of thermal radiation.

The trade-off is explicit: the present method eliminates the need for absolute intensity calibration and active probes, at the cost of requiring knowledge of the medium response function $\sigma(\omega)$ and stable relative calibration between electric and magnetic detection channels. In applications where $\sigma(\omega)$ can be independently measured (e.g., from reflectivity or Thomson scattering on the medium at rest), this trade-off is favorable.

Beyond diagnostic capability, there is a qualitative distinction: the present protocol is the only method that

TABLE I. Comparison of relativistic thermal diagnostics.

Requirement	Radiometry	Thomson	This work
Active probe	No	Yes	No
Absolute intensity cal.	Yes	Yes	No
Spectral lines needed	Often	No	No
Independent β meas.	Yes ^a	Fit ^b	No ^c
$\sigma(\omega)$ knowledge	No	No	Yes
Relative E/B cal.	N/A	N/A	Yes
Unified β^μ output	No ^d	No ^d	Yes

^aRadiometry of a moving source yields $T_0/D(\theta)$; disentangling T_0 from β requires independent velocity information (e.g., Doppler shift of spectral lines).

^bThomson scattering fits velocity and temperature simultaneously from the scattered spectrum, but requires an external laser and absolute spectral calibration.

^cVelocity is extracted from the E - B cross-correlation within the same passive measurement.

^d T_0 and β are inferred from different observables or different physical mechanisms and assembled into β^μ post hoc.

outputs β^μ as a unified observable reconstructed from a single measurement channel. All other techniques assemble β^μ from separate measurements of T_0 and u^μ , each carrying independent systematic uncertainties and model assumptions. The angular consistency check—whether $T_0^{\text{(rec)}}(\theta)$ is flat across all pixels when the correct β is used—provides a direct test of the four-vector transformation law that is unavailable when T_0 and β come from different instruments.

VI. NUMERICAL VALIDATION WITH LASER-PLASMA PARAMETERS

We validate the reconstruction protocol using Monte Carlo simulations parameterized to the HIGGINS dual 100 TW laser-plasma facility at the Weizmann Institute of Science [22]. The underlying physics—the covariant FDT and Lorentz transformation of thermal radiation—is well established; the simulations do not test these foundations but rather characterize the *statistical precision and noise robustness* of the proposed measurement protocol under realistic experimental parameters. This system produces ultrarelativistic electron bunches with Lorentz factors $\gamma \sim 1$ –10 via laser wakefield acceleration in a nitrogen supersonic gas jet ($n_e \approx 10^{19} \text{ cm}^{-3}$), providing a concrete setting in which the proposed diagnostic can be implemented with existing infrastructure.

A. Simulation model

The simulation generates an ensemble of $N_{\text{mode}} = 4 \times 10^4$ thermal electromagnetic modes in the rest frame of the plasma, uniformly distributed in direc-

tion (isotropic) and frequency $\omega \in [0.1, 13.0] \omega_p$, where $\omega_p = (n_e e^2 / \epsilon_0 m_e)^{1/2} \approx 1.78 \times 10^{14} \text{ rad/s}$ ($f_p \approx 28 \text{ THz}$, $\lambda_p \approx 10.6 \mu\text{m}$). Mode amplitudes are drawn from the classical fluctuation–dissipation theorem with a Drude conductivity $\sigma(\omega) = \nu / (\nu^2 + \omega^2)$, collision frequency $\nu / \omega_p = 0.05$, and electron temperature $T_0 = 1 \text{ keV}$ ($k_B T_0 / \hbar \omega_p = 8512$, deep in the classical regime). Each mode carries two independently drawn random polarizations with complex Gaussian amplitudes whose variance is $\langle |a|^2 \rangle \propto T_0 \sigma(\omega)$.

All modes are Lorentz-boosted to the laboratory frame at velocity βc , transforming frequencies via $\omega' = \omega / D(\theta)$ and field components via Eqs. (5)–(6). A detector array of 12 pixels uniformly spaced from $\theta_{\text{lab}} = 15^\circ$ to 165° in a ring at distance $R = 50 \text{ cm}$ (far field: $R / \lambda_p \approx 4.7 \times 10^4 \gg 1$), with pixel size $d = 3 \text{ cm}$ ($\Delta\theta = 3.4^\circ$), bins the boosted modes by laboratory angle. The y -component of the electric field at each pixel yields a power spectral density from which the total pixel power $W(\theta)$ is computed. The velocity β_{EB} is independently recovered from the E - B cross-correlation ratio, Eq. (10).

B. Two-step calibration protocol

The measurement proceeds in two steps. In Step 1 (calibration), the plasma is measured at rest ($\beta = 0$). The angular power pattern $W_{\text{rest}}(\theta) \propto \sin\theta \cdot P_{E_y}(\theta, 0) \cdot \int \sigma(\omega) d\omega$ encodes the product of the mode density (the $\sin\theta$ factor from the solid-angle Jacobian), the azimuth-averaged polarization projection $P_{E_y}(\theta, 0) = (1 + \cos^2\theta)/2$, and the integrated conductivity. This provides an absolute reference that anchors the amplitude scale.

In Step 2, the plasma is boosted (or equivalently, the detector observes a drifting plasma). The laboratory-frame power at each pixel is

$$W_{\text{lab}}(\theta) \propto \frac{\sin\theta}{D^2(\theta)} P_{E_y}(\theta, \beta) T_0 \int \sigma(D\omega') d\omega', \quad (18)$$

where $D(\theta) = \gamma(1 - \beta \cos\theta)$ and $P_{E_y}(\theta, \beta)$ is the exact azimuth-averaged polarization factor. The ratio $W_{\text{lab}}(\theta) / W_{\text{rest}}(\theta)$ eliminates the calibration-dependent amplitude. In the high-frequency regime $\omega \gg \nu$ where $\sigma(\omega) \approx \nu / \omega^2$, the integral ratio $\int \sigma(D\omega') d\omega' / \int \sigma(\omega) d\omega \rightarrow D^{-1}$, and the ratio becomes a function of (β, θ) alone, from which $T_{\text{lab}}(\theta) = T_0 / D(\theta)$ is extracted at each pixel using β_{EB} from the E - B correlation. If the detection bandwidth extends to $\omega \lesssim \nu$, the integral ratio retains residual σ -dependence that must be modeled; for the HIGGINS parameters ($\nu / \omega_p = 0.05$, $\omega_{\text{min}} = 0.1 \omega_p$), this correction is at the sub-percent level.

C. Single- γ temperature extraction

Figure 1 shows results for $\gamma = 1.5$ ($\beta = 0.745$), characteristic of electron bunches produced by HIGGINS. The simulation uses 10^4 ensemble realizations with 4×10^4 modes each. The angular temperature profile $T_{\text{lab}}(\theta)$ is recovered at 12 detector pixels spanning $\theta = 15^\circ$ to 165° .

The measured temperatures agree with the theoretical prediction $T_{\text{lab}}(\theta) = T_0/D(\theta)$ to within 0.34% RMS across all pixels. The forward pixel ($\theta = 15^\circ$) measures $T_{\text{lab}} \approx 20,000 \hbar\omega_p$ while the backward pixel ($\theta = 165^\circ$) measures $T_{\text{lab}} \approx 3,000 \hbar\omega_p$, spanning a factor of ~ 7 in apparent temperature—a direct manifestation of the relativistic Doppler factor in the covariant thermal state. The velocity is independently recovered as $\beta_{\text{EB}} = 0.746 \pm 0.017$ from the E - B cross-correlation, consistent with the injected value.

The flatness of the recovered rest-frame temperature $T_0^{(\text{rec})}(\theta)$ across all pixels constitutes a self-consistency test of the four-vector structure: if β^μ did not transform as a Lorentz four-vector, the angular profile would not reduce to a uniform T_0 upon division by $D(\theta)$. This consistency check is intrinsic to the protocol and requires no additional measurements.

D. Multi- γ robustness

To demonstrate that the protocol is not tuned to a particular Lorentz factor, we repeat the extraction for eight values spanning $\gamma \in \{1.05, 1.1, 1.2, 1.5, 2, 3, 5, 10\}$, using a shared calibration run ($\beta = 0$, 10^3 realizations) and 10^3 boosted realizations per γ (Fig. 2).

The rest-frame temperature T_0 is recovered to sub-percent accuracy for $\gamma \leq 2$, degrading to $\sim 2\%$ at $\gamma = 3$ and $\sim 6\%$ at $\gamma = 10$. This degradation is physical, not methodological: at high γ , relativistic beaming concentrates radiation into a narrow forward cone, starving backward-angle pixels of modes (average modes per pixel: 831 at $\gamma = 1.05$ versus 223 at $\gamma = 10$). The Lorentz factor is independently recovered from the E - B cross-correlation to within error bars across the full range (Fig. 2b).

E. Noise susceptibility

Experimental implementation requires robustness against detector noise. We model additive noise as a flat power floor $P_{\text{noise}} = \langle P_{\text{signal}} \rangle / \text{SNR}$ added to each pixel, with pixel-level fluctuations drawn from an exponential distribution (appropriate for chi-squared distributed power measurements). Two scenarios are compared: raw recovery (no noise correction) and noise-subtracted recovery, in which a separately measured dark frame is subtracted (Fig. 3).

Without subtraction, the noise floor biases T_0 upward because excess power mimics higher temperature. The

bias scales as $\sim 100/\text{SNR} \%$. With dark subtraction, the systematic bias is eliminated and the dominant error is pixel-to-pixel scatter from noise fluctuations. For $\gamma = 1.5$, the total recovery error (RMS) remains below 10% for $\text{SNR} \gtrsim 10$ with subtraction, compared to $\text{SNR} \gtrsim 50$ without. At $\gamma = 3$, mode starvation at backward angles amplifies the noise sensitivity, and $\text{SNR} \gtrsim 50$ is needed for comparable accuracy.

These thresholds are well within the capabilities of mid-infrared bolometer arrays operating at $\lambda \sim 10 \mu\text{m}$.

VII. EXPERIMENTAL IMPLEMENTATION

The HIGGINS system [22] delivers two independently compressed 100 TW pulses (7 J split, 30 fs, 800 nm) focused to $\sim 28 \mu\text{m}$ spots onto a nitrogen supersonic gas jet of $\sim 3 \text{ mm}$ diameter. After laser-plasma interaction, the electron population thermalizes on sub-picosecond timescales with $T_e \sim 1 \text{ keV}$ and plasma frequency $\omega_p \approx 28 \text{ THz}$.

The proposed diagnostic requires a ring of ~ 12 mid-infrared detectors (e.g., MCT or pyroelectric bolometers sensitive at $\lambda \sim 10 \mu\text{m}$) placed at $R \approx 50 \text{ cm}$ from the plasma source, covering angles from 15° to 165° relative to the electron drift direction. Each pixel integrates over a $\sim 3 \text{ cm}$ aperture ($\Delta\theta \approx 3.4^\circ$). The E - B cross-correlation for velocity extraction (Eq. 10) can be measured using dual-polarization detection or split-path pickup combining electric and magnetic antenna feeds, as routinely implemented in microwave polarimetry and plasma interferometry [10].

The two-step protocol (Sec. VIB) requires one calibration shot with the plasma at rest (or at known low drift) and subsequent shots with the plasma boosted. Since HIGGINS operates at 1 Hz repetition rate [22], ensemble averaging over $\sim 10^3$ shots requires ~ 15 minutes per γ setting. The simulations demonstrate that 10^3 realizations suffice for sub-percent T_0 recovery at $\gamma = 1.5$ (Fig. 1).

VIII. SYSTEMATIC UNCERTAINTIES AND LIMITATIONS

The dominant systematic uncertainties are:

1. *Relative channel calibration.* The velocity extraction via Eq. (10) depends on the relative calibration of the electric and magnetic detection channels. A multiplicative error α in the relative gain ($B'_x \rightarrow \alpha B'_x$) shifts the measured ratio to $R_{\text{meas}} = \alpha R$, producing a systematic velocity error $\delta\beta/\beta \approx \alpha - 1$ at low β . This can be characterized *in situ* by injecting a known test signal or by measuring the ratio on a source at known velocity.
2. *Medium response function.* The temperature extraction via Eq. (16) requires knowledge of the

- conductivity $\sigma(\omega)$. In the high-frequency regime $\omega \gg \nu$ relevant to the HIGGINS parameters, $\sigma(\omega) \approx \nu/\omega^2$; the PSD then scales as $T_0 \nu/\omega^2$, and only the product $T_0 \nu$ is constrained by the spectral shape. The rest-frame temperature T_0 is therefore not independently determined by the fluctuation measurement alone unless $\sigma(\omega)$ is independently characterized—a standard prerequisite for any plasma diagnostic. In practice, the conductivity is a material property that can be measured once (e.g., via reflectivity, Thomson scattering, or Langmuir-probe analysis on the medium at rest [9, 10]) or obtained from tabulated data; after which the fluctuation measurement determines β^μ without further auxiliary input. In the high-frequency regime a fractional error $\delta\sigma/\sigma$ in the conductivity propagates linearly into the recovered temperature: $\delta T_0/T_0 \approx \delta\sigma/\sigma$. Crucially, such an error shifts $T_0^{(\text{rec})}(\theta)$ uniformly across all angles without introducing angular structure, and leaves the velocity estimator β_{EB} unchanged (Fig. 4, panels c–d). This angular uniformity provides a diagnostic: a misidentified $\sigma(\omega)$ can be distinguished from a genuine anisotropy (item 4) by the absence of angular trends in $T_0^{(\text{rec})}(\theta)$.
3. *Rest-frame calibration requirements.* The two-step protocol (Sec. VIB) requires a calibration measurement at $\beta = 0$ or at a known low drift β_{cal} . In a laser-wakefield system, achieving $\beta_{\text{cal}} = 0$ exactly while maintaining identical plasma conditions (n_e , T_0 , ν) is nontrivial. A residual calibration velocity $\beta_{\text{cal}} \neq 0$ introduces a systematic error in the power ratio: the calibration pattern acquires factors of $D_{\text{cal}}(\theta)$ and $P_{E_y}(\theta, \beta_{\text{cal}})$ that, if unaccounted for, bias the extracted temperature. For $\beta_{\text{cal}} \ll 1$, the leading error is $\delta T_0/T_0 \sim \beta_{\text{cal}} \cos \theta$, which averages partially over the angular array but does not cancel. The calibration velocity must therefore either be independently measured (e.g., from the E – B ratio on the calibration data itself) or kept below the target accuracy. For sub-percent T_0 recovery, this requires $\beta_{\text{cal}} \lesssim 0.01$.
 4. *Departure from isotropy.* The velocity extraction (Eq. 10) relies on the rest-frame isotropy condition $\langle \delta E_y \delta B_x^* \rangle_{\text{rest}} = 0$. If the rest-frame fluctuations are anisotropic—for example, due to beam-driven instabilities, an anisotropic electron distribution, or residual laser fields—the rest-frame E – B correlation acquires a nonzero value $\langle \delta E_y \delta B_x^* \rangle_{\text{rest}} = \epsilon \langle |E_y|^2 \rangle$ with $|\epsilon| \ll 1$. Propagating this through the boost, the measured ratio becomes $R = 2\beta/(1 + \beta^2) + \epsilon(1 - \beta^2)/(1 + \beta^2)^2 + O(\epsilon^2)$, where the suppression relative to ϵ arises because the anisotropy injection modifies both the numerator and denominator of the ratio. The velocity estimator acquires a systematic shift $\delta\beta \approx \epsilon(1 - \beta^2)/2 = \epsilon/(2\gamma^2)$ at leading order. An anisotropy at the 1% level

($\epsilon \sim 0.01$) would bias β by ~ 0.002 at $\gamma = 1.5$ —comparable to the statistical uncertainty at 10^3 realizations. The angular temperature profile provides an independent consistency check: if the rest frame is misidentified due to anisotropy, the recovered $T_0^{(\text{rec})}(\theta)$ will show systematic angular trends rather than the flat profile expected for correct β . Adversarial Monte Carlo simulations confirm both effects quantitatively (Fig. 4): injecting rest-frame anisotropy at the $\epsilon = 1$ –5% level produces velocity biases $\delta\beta \approx \epsilon/(2\gamma^2)$ and angular trends in $T_0^{(\text{rec})}(\theta)$ that serve as internal diagnostics, while conductivity mismatches of $\pm 20\%$ shift T_0 uniformly without affecting β_{EB} . The two failure modes are therefore experimentally distinguishable.

5. *Shot-to-shot variation.* Laser-plasma systems exhibit stochastic fluctuations in electron density, temperature, and bunch parameters between shots. The ensemble averaging inherent in the protocol mitigates this, provided the mean plasma state is stationary over the integration window.
6. *Departure from thermal equilibrium.* The temperature reconstruction assumes local thermodynamic equilibrium in the comoving frame. Non-thermal features such as beam-generated instabilities or coherent plasma emission would appear as excess power at specific angles or frequencies. Such features would degrade the fit to the smooth angular profile predicted by Eq. (16), and their presence can be diagnosed from the residuals of the $T_0^{(\text{rec})}(\theta)$ extraction.

IX. DISCUSSION

The protocol presented here reconstructs the inverse-temperature four-vector β^μ of a relativistic equilibrium medium from passive electromagnetic fluctuation measurements—something no existing diagnostic achieves as a unified observable. The velocity is extracted from the E – B cross-correlation ratio, which accesses the off-diagonal sector of the boosted field-strength tensor $F^{\mu\rho}$ and has no counterpart in standard radiometry or Stokes polarimetry. The temperature is extracted from the angular dependence of the noise power via a ratio method that cancels absolute calibration factors. Together, these yield both components of β^μ from a single passive field measurement, without the post hoc assembly of separately measured quantities that characterizes all existing approaches.

The method does not introduce new fundamental physics: the Lorentz transformation of thermal radiation and the covariant FDT are well established [7, 11]. The contribution is operational—the identification of specific observables and a measurement protocol that provides the first direct experimental access to β^μ as a unified

quantity. The trade-off relative to conventional diagnostics is explicit: the method eliminates absolute intensity calibration and active probes, at the cost of requiring knowledge of $\sigma(\omega)$ and stable relative E/B channel calibration.

A further consequence deserves emphasis. The Planck–Ott–Landsberg controversy over how temperature transforms under Lorentz boosts was resolved theoretically by the recognition that the thermal state is described by β^μ , not a scalar temperature [1, 4, 5]. But this resolution has remained purely theoretical: no experiment has ever measured the thermal state of a relativistic medium at multiple angles and verified that the resulting $T_{\text{lab}}(\theta)$ profile is consistent with a single four-vector β^μ . The angular consistency check built into the present protocol—the flatness of $T_0^{(\text{rec})}(\theta)$ across all detector pixels—provides exactly this test. If the thermal state did not transform as a four-vector, the angular profile would not reduce to a uniform rest-frame temperature upon division by $D(\theta)$.

Monte Carlo simulations parameterized to the HIGGINS dual 100 TW laser-plasma facility demonstrate sub-percent accuracy for $\gamma \leq 2$ and robustness to additive detector noise at $\text{SNR} \gtrsim 10$ with dark subtraction. The required hardware—a ring of mid-infrared bolometers at $\lambda \sim 10 \mu\text{m}$ —is commercially available and compatible with existing laser-plasma experimental infrastructure. The principal experimental challenges are maintaining rest-frame isotropy (Sec. VIII, item 4), achieving adequate E – B channel stability, and independently characterizing $\sigma(\omega)$, a standard prerequisite for any plasma diagnostic. Adversarial simulations (Fig. 4)

demonstrate that these two failure modes—rest-frame anisotropy and conductivity mismatch—produce distinct signatures in the angular profile and can be diagnosed internally without auxiliary measurements.

The method is most immediately applicable to controlled laboratory settings—laser-produced plasmas, beam–plasma systems, and magnetically confined plasmas with $E \times B$ drift—where equilibrium can be maintained and angular access is unrestricted. These are precisely the systems in which the covariant thermal structure can be verified for the first time. The broader significance is sequential. In relativistic heavy-ion collisions, “temperature” is routinely extracted from particle spectra under the assumption that the thermal state transforms as a four-vector β^μ , but this assumption has never been independently verified—it is built into the analysis framework, not tested by it. A controlled laboratory measurement that confirms (or falsifies) the four-vector transformation law provides the empirical baseline against which heavy-ion thermal analyses can be assessed. Similarly, in astrophysical contexts such as gamma-ray bursts, the principle of extracting thermal parameters from passive fluctuation statistics could inform single-sightline spectral analyses, though adapting the present multi-angle protocol to single-line-of-sight observations would require further theoretical development. The laboratory measurement is therefore not merely a proof of concept: it is the necessary first link in a chain that extends from plasma diagnostics to high-energy nuclear physics and relativistic astrophysics.

-
- [1] F. Becattini, *Phys. Rev. Lett.* **117**, 192301 (2016).
 [2] L. Gavassino, *Class. Quantum Grav.* **39**, 185008 (2022).
 [3] D. N. Zubarev, *Nonequilibrium Statistical Thermodynamics* (Consultants Bureau, New York, 1974).
 [4] N. G. van Kampen, *Phys. Rev.* **173**, 295 (1968).
 [5] W. Israel and J. M. Stewart, *Ann. Phys. (N.Y.)* **118**, 341 (1979).
 [6] C. Cercignani and G. M. Kremer, *The Relativistic Boltzmann Equation: Theory and Applications* (Birkhäuser, Basel, 2002).
 [7] J. I. Kapusta and C. Gale, *Finite-Temperature Field Theory: Principles and Applications* (Cambridge University Press, 2nd ed., 2006).
 [8] M. Le Bellac, *Thermal Field Theory* (Cambridge University Press, 1996).
 [9] J. Sheffield, D. Froula, S. H. Glenzer, and N. C. Luhmann, *Plasma Scattering of Electromagnetic Radiation* (Academic Press, 2nd ed., 2011).
 [10] I. H. Hutchinson, *Principles of Plasma Diagnostics* (Cambridge University Press, 2nd ed., 2002).
 [11] G. B. Rybicki and A. P. Lightman, *Radiative Processes in Astrophysics* (Wiley, 1979).
 [12] W. Busza, K. Rajagopal, and W. van der Schee, *Annu. Rev. Nucl. Part. Sci.* **68**, 339 (2018).
 [13] P. Kumar and B. Zhang, *Phys. Rep.* **561**, 1 (2015).
 [14] M. Planck, *Ann. Phys. (Leipzig)* **26**, 1 (1908).
 [15] H. Ott, *Z. Phys.* **175**, 70 (1963).
 [16] P. T. Landsberg, *Nature* **212**, 571 (1966).
 [17] K. Issautier, N. Meyer-Vernet, M. Moncuquet, S. Hoang, and D. J. McComas, *J. Geophys. Res.* **104**, 6691 (1999).
 [18] C. Ruyer, L. Gremillet, D. Bénisti, and G. Bonnaud, *Phys. Plasmas* **20**, 112104 (2013); arXiv:1310.7721.
 [19] J. B. Johnson, *Phys. Rev.* **32**, 97 (1928).
 [20] H. Nyquist, *Phys. Rev.* **32**, 110 (1928).
 [21] H. B. Callen and T. A. Welton, *Phys. Rev.* **83**, 34 (1951).
 [22] E. Kroupp, S. Tata, Y. Wan, D. Levy, S. Smartsev, E. Y. Levine, O. Seemann, M. Adelberg, R. Piliposian, T. Queller, E. Segre, K. Ta Phuoc, M. Kozlova, and V. Malka, *Matter Radiat. Extremes* **7**, 044401 (2022).
 [23] F. Jüttner, *Ann. Phys. (Leipzig)* **339**, 856 (1911).
 [24] P. T. Landsberg and G. E. A. Matsas, *Phys. Lett. A* **223**, 401 (1996).
 [25] R. Kubo, *Rep. Prog. Phys.* **29**, 255 (1966).

Appendix A: Derivation of the laboratory-frame PSD

This appendix derives Eq. (16) from first principles, tracking all frequency-dependent prefactors through the Lorentz transformation. Standard textbook references for the individual ingredients are Rybicki & Lightman [11] (radiative transfer and Lorentz invariance of I_ν/ν^3) and Kapusta & Gale [7] (finite-temperature field theory and the covariant FDT).

1. Rest-frame PSD with all prefactors

In Sec. III A we showed that the electric-field PSD in the rest frame follows from projecting the covariant FDT onto the transverse electric component. The projection involves two steps: (i) the current fluctuations $\Pi_S^{\mu\rho}$ source electric fields through Maxwell's equations, introducing a factor $\omega^2/|\epsilon(\omega)|^2$; (ii) the dissipative response satisfies $\text{Im}\Pi_R^i(\omega) \propto \omega\sigma(\omega)$, where $\sigma(\omega)$ is the real part of the conductivity. Combining with the covariant FDT, Eq. (12), the full rest-frame PSD is

$$S_E^{(\text{rest})}(\omega) = C \frac{\omega^2}{|\epsilon(\omega)|^2} \coth\left(\frac{\hbar\omega}{2k_B T_0}\right) \omega \sigma(\omega), \quad (\text{A1})$$

where C collects frequency-independent geometric constants.

2. Classical limit

In the regime $\hbar\omega \ll k_B T_0$, the coth factor simplifies:

$$\coth\left(\frac{\hbar\omega}{2k_B T_0}\right) \xrightarrow{\hbar\omega \ll k_B T_0} \frac{2k_B T_0}{\hbar\omega}. \quad (\text{A2})$$

Substituting into Eq. (A1), the $1/\omega$ from the classical coth cancels against one power of ω from the dissipative response:

$$S_E^{(\text{rest})}(\omega) = \frac{2Ck_B T_0}{\hbar} \frac{\omega^2 \sigma(\omega)}{|\epsilon(\omega)|^2}. \quad (\text{A3})$$

The factor $T_0 \sigma(\omega)$ carries the thermal and material content. The factor $\omega^2/|\epsilon(\omega)|^2$ is a density-of-states prefactor from the electromagnetic projection. In the rest frame, one may absorb the latter into a proportionality constant, since it cancels in ratio observables. However, because ω^2 transforms nontrivially under a Lorentz boost, *this prefactor must be retained when changing frames.*

3. Doppler relation

Let the medium drift at velocity $v = \beta c$ relative to the laboratory, and let θ be the angle between the labora-

tory photon propagation direction \hat{k}' and the drift velocity $\hat{\beta}$. The Lorentz transformation of the photon four-momentum $p^\mu = (\omega/c, \mathbf{k})$ gives the relativistic Doppler relation [11]:

$$\omega = D \omega', \quad D \equiv \gamma(1 - \beta \cos\theta), \quad (\text{A4})$$

where $\gamma = (1 - \beta^2)^{-1/2}$ is the Lorentz factor. Here ω is the rest-frame frequency and ω' the laboratory frequency. The Doppler factor D satisfies $D < 1$ for radiation approaching the observer (blueshift) and $D > 1$ for radiation receding (redshift).

4. Lorentz invariance of I_ν/ν^3

The key tool for transforming spectral quantities between frames is the Lorentz invariance of the photon phase-space distribution function f . This follows from the fact that f counts the number of photons per cell in single-particle phase space, and both the phase-space volume element $d^3x d^3p$ and the photon number are Lorentz invariants.

The specific intensity (energy per unit time, per unit area, per unit frequency, per unit solid angle) is related to f by (see Rybicki & Lightman [11], §4.9):

$$I_\nu = \frac{2h\nu^3}{c^2} f. \quad (\text{A5})$$

Since f is a Lorentz scalar, the ratio I_ν/ν^3 is Lorentz invariant:

$$\frac{I_{\nu'}(\nu')}{\nu'^3} = \frac{I_\nu^{(\text{rest})}(\nu)}{\nu^3}. \quad (\text{A6})$$

5. Transformation of the PSD

The electric-field PSD S_E is proportional to I_ν : both quantify the spectral energy flux per unit frequency per unit solid angle. Therefore, the invariance of I_ν/ν^3 implies

$$\frac{S_E(\omega', \theta)}{\omega'^3} = \frac{S_E^{(\text{rest})}(\omega)}{\omega^3}, \quad (\text{A7})$$

which gives the transformation rule

$$S_E(\omega', \theta) = \left(\frac{\omega'}{\omega}\right)^3 S_E^{(\text{rest})}(\omega) = D^{-3} S_E^{(\text{rest})}(\omega). \quad (\text{A8})$$

This is the relativistic beaming factor: radiation is enhanced ($D^{-3} > 1$) toward the observer and suppressed ($D^{-3} < 1$) away from it. The cubic power reflects the combined effect of time dilation, solid-angle aberration, and frequency shift.

6. Combining the ingredients

Substituting the classical rest-frame PSD, Eq. (A3), into the transformation rule, Eq. (A8), and replacing every occurrence of ω by $D\omega'$:

$$\begin{aligned} S_E(\omega', \theta) &= D^{-3} \frac{2Ck_B T_0}{\hbar} \frac{(D\omega')^2 \sigma(D\omega')}{|\epsilon(D\omega')|^2} \\ &= D^{-3} \cdot D^{+2} \frac{2Ck_B T_0}{\hbar} \frac{\omega'^2 \sigma(D\omega')}{|\epsilon(D\omega')|^2}. \end{aligned} \quad (\text{A9})$$

The powers of D collect as

$$\underbrace{D^{-3}}_{\text{beaming}} \times \underbrace{D^{+2}}_{\omega^2 \text{ prefactor}} = D^{-1}. \quad (\text{A10})$$

The physical content: the D^{-3} beaming factor would, on its own, produce a strong angular modulation. But the medium's response σ is sampled at a Doppler-shifted frequency, and the ω^2 density-of-states factor (which came from projecting $\Pi_S^{\mu\rho}$ onto the electric field via Maxwell's equations) partially compensates the beaming. The net surviving power is D^{-1} .

The remaining factor $\omega'^2/|\epsilon(D\omega')|^2$ depends only on the laboratory frequency and the material response. In the ratio observables constructed in the main text (Sec. VIB), these factors cancel between numerator and denominator. Absorbing them into a proportionality, we arrive at the laboratory-frame PSD:

$$S(\omega', \theta) \propto \frac{T_0}{D} \sigma(D\omega') = \frac{T_0}{\gamma(1 - \beta \cos \theta)} \sigma(\gamma\omega'(1 - \beta \cos \theta)). \quad (\text{A11})$$

This is Eq. (16) of the main text.

Appendix B: Simulation algorithm

This appendix provides the complete simulation algorithm used in Sec. VI, sufficient for independent reproduction without reference to the accompanying code repository.

1. Mode generation in the rest frame

Each realization generates N_{mode} electromagnetic plane-wave modes in the comoving frame. For mode n ($n = 1, \dots, N_{\text{mode}}$):

1. Draw frequency ω_n uniformly from $[\omega_{\min}, \omega_{\max}]$.
2. Draw propagation direction \hat{k}_n isotropically on the unit sphere by sampling $\cos \theta_n^{(\text{rest})}$ uniformly from $[-1, +1]$ and azimuth ϕ_n uniformly from $[0, 2\pi)$. The Cartesian wave-vector components are

$$\hat{k}_n = (\sin \theta_n \cos \phi_n, \sin \theta_n \sin \phi_n, \cos \theta_n). \quad (\text{B1})$$

The uniform sampling in $\cos \theta$ ensures isotropic mode density on the sphere. This is the origin of the $\sin \theta$ factor in the angular power pattern.

3. Construct two orthonormal polarization basis vectors $\hat{e}_{1,n}$ and $\hat{e}_{2,n}$ perpendicular to \hat{k}_n . We choose

$$\hat{e}_{1,n} = \frac{\hat{z} \times \hat{k}_n}{|\hat{z} \times \hat{k}_n|} \quad (\text{B2})$$

when $|\hat{z} \times \hat{k}_n| > \varepsilon$ (with $\varepsilon = 0.1$ to avoid the pole), and $\hat{e}_{1,n} = (\hat{y} \times \hat{k}_n)/|\hat{y} \times \hat{k}_n|$ otherwise. The second vector is $\hat{e}_{2,n} = \hat{k}_n \times \hat{e}_{1,n}$.

4. Assign complex amplitudes to each polarization:

$$\begin{aligned} a_{1,n} &= A_n (g_{1,n} + i g_{2,n}), \\ a_{2,n} &= A_n (g_{3,n} + i g_{4,n}), \end{aligned} \quad (\text{B3})$$

where $g_{j,n} \sim \mathcal{N}(0, 1)$ are independent standard normal variates and the envelope amplitude is

$$A_n = \sqrt{\frac{T_0 \sigma(\omega_n)}{N_{\text{mode}}}}, \quad (\text{B4})$$

with $\sigma(\omega) = \nu/(\nu^2 + \omega^2)$ the Drude conductivity. The factor $1/N_{\text{mode}}$ ensures that the ensemble-averaged total power converges as $N_{\text{mode}} \rightarrow \infty$. The variance of each complex amplitude satisfies $\langle |a_{j,n}|^2 \rangle = 2A_n^2 \propto T_0 \sigma(\omega_n)$, implementing the classical FDT.

5. Construct the rest-frame electric and magnetic field vectors for mode n :

$$\mathbf{E}_n = a_{1,n} \hat{e}_{1,n} + a_{2,n} \hat{e}_{2,n}, \quad (\text{B5})$$

$$\mathbf{B}_n = \hat{k}_n \times \mathbf{E}_n. \quad (\text{B6})$$

Here $\mathbf{B}_n = \hat{k}_n \times \mathbf{E}_n$ follows from Maxwell's equations for a plane wave with $|\mathbf{B}| = |\mathbf{E}|/c$, in units where $c = 1$.

2. Lorentz boost

For a boost along \hat{z} with velocity β and Lorentz factor $\gamma = (1 - \beta^2)^{-1/2}$, the laboratory-frame fields are

$$\begin{aligned} E'_{x,n} &= \gamma(E_{x,n} - \beta B_{y,n}), \\ E'_{y,n} &= \gamma(E_{y,n} + \beta B_{x,n}), \\ E'_{z,n} &= E_{z,n}, \\ B'_{x,n} &= \gamma(B_{x,n} + \beta E_{y,n}), \\ B'_{y,n} &= \gamma(B_{y,n} - \beta E_{x,n}), \\ B'_{z,n} &= B_{z,n}, \end{aligned} \quad (\text{B7})$$

and the laboratory-frame propagation angle follows from relativistic aberration:

$$\cos \theta_n^{(\text{lab})} = \frac{\cos \theta_n^{(\text{rest})} + \beta}{1 + \beta \cos \theta_n^{(\text{rest})}}. \quad (\text{B8})$$

3. Pixel binning

The detector array consists of N_{pix} pixels at laboratory angles θ_i ($i = 1, \dots, N_{\text{pix}}$) with half-width $\Delta\theta/2$. Mode n is assigned to pixel i if $|\theta_n^{(\text{lab})} - \theta_i| \leq \Delta\theta/2$.

The pixel power in the y -polarization channel is

$$W_i = \sum_{n \in \text{pixel } i} |E'_{y,n}|^2. \quad (\text{B9})$$

4. Angular power model

The expected pixel power involves three angular factors whose origins are distinct:

1. *Mode density:* The number of isotropically generated modes falling within pixel i is proportional to the solid angle subtended, $\Delta\Omega_i \propto \sin\theta_i \Delta\theta$. Under the boost, the aberration Jacobian $d(\cos\theta_{\text{rest}})/d(\cos\theta_{\text{lab}}) = D^{-2}$ modifies the effective mode density per unit laboratory angle to $\propto \sin\theta_i/D^2(\theta_i)$. However, each mode's frequency is Doppler-shifted by $\omega' = \omega/D$, so the frequency integration $\int \sigma(D\omega') d\omega'$ recovers one power of D , yielding a net mode-density factor $\sin\theta_i/D(\theta_i)$.
2. *Polarization projection:* The y -component of the electric field is $E'_y = \mathbf{E}' \cdot \hat{y}$, a projection that depends on the mode direction and boost. The azimuth-averaged projection factor is

$$P_{E_y}(\theta, \beta) = \left\langle \frac{|E'_y|^2}{|\mathbf{E}'|^2/2} \right\rangle_{\phi}, \quad (\text{B10})$$

where $\langle \cdot \rangle_{\phi}$ denotes averaging over the azimuthal angle of the mode propagation direction at fixed polar angle θ . In the rest frame ($\beta = 0$), this reduces to

$$P_{E_y}(\theta, 0) = \frac{1 + \cos^2\theta}{2}, \quad (\text{B11})$$

which varies from 1 at the poles to 1/2 at the equator. This factor is *not* the isotropic average 2/3; using the full-sphere average instead of the angle-dependent expression introduces systematic errors of up to 45% at forward and backward angles.

For $\beta > 0$, $P_{E_y}(\theta, \beta)$ must be computed by performing the azimuth average of the boosted field projection numerically. For each laboratory angle θ_{lab} : (i) compute the rest-frame angle via the inverse of Eq. (B8); (ii) for N_{ϕ} azimuthal samples ϕ_j uniformly distributed in $[0, 2\pi)$, construct the rest-frame propagation direction and polarization basis, boost the fields, and compute $|E'_y|^2$; (iii) average over ϕ_j . We use $N_{\phi} = 300$, which yields convergence to better than 0.1% in P_{E_y} at all angles and Lorentz factors considered; doubling N_{ϕ} changes the result by less than 10^{-4} .

3. *Spectral weight:* Each mode contributes power $\propto T_0 \sigma(\omega_n)$. After the boost, the conductivity is sampled at the Doppler-shifted frequency $\sigma(D\omega')$.

Combining these factors, the expected pixel power is

$$\langle W_i \rangle \propto \frac{\sin\theta_i}{D(\theta_i)} P_{E_y}(\theta_i, \beta) T_0 \int \sigma(D\omega') d\omega'. \quad (\text{B12})$$

5. Velocity extraction from the E - B cross-correlation

The velocity is extracted from the full set of boosted modes (not binned by pixel). Define the mode-sum estimator

$$\hat{R} = \frac{\text{Re} \left[\sum_{n=1}^{N_{\text{mode}}} E'_{y,n} B_{x,n}^{*} \right]}{\sum_{n=1}^{N_{\text{mode}}} |E'_{y,n}|^2}, \quad (\text{B13})$$

which estimates $R = 2\beta/(1 + \beta^2)$ from Eq. (10). The velocity is recovered by inversion:

$$\beta_{\text{EB}} = \frac{1 - \sqrt{1 - \hat{R}^2}}{\hat{R}}. \quad (\text{B14})$$

This estimator is formed from a single realization; ensemble averaging of β_{EB} over N_{ens} realizations reduces the statistical uncertainty as $1/\sqrt{N_{\text{ens}}}$.

6. Two-step calibration and temperature extraction

- Step 1: Rest-frame calibration.* Run N_{cal} realizations with $\beta = 0$. The ensemble-averaged pixel power is

$$\bar{W}_{\text{rest}}(\theta_i) = \frac{1}{N_{\text{cal}}} \sum_{k=1}^{N_{\text{cal}}} W_i^{(k)} \Big|_{\beta=0}. \quad (\text{B15})$$

This measures the product of calibration constants and the angular pattern $\sin\theta_i \cdot P_{E_y}(\theta_i, 0) \cdot \int \sigma d\omega$.

- Step 2: Boosted measurement.* Run N_{boost} realizations at velocity β . The ensemble-averaged pixel power is $\bar{W}_{\text{lab}}(\theta_i)$. Using β_{EB} from Eq. (B14), compute the Doppler factor $D_i = \gamma_{\text{EB}}(1 - \beta_{\text{EB}} \cos\theta_i)$ and the polarization factors $P_{E_y}(\theta_i, \beta_{\text{EB}})$ and $P_{E_y}(\theta_i, 0)$ at each pixel.

- Temperature inversion.* The ratio of boosted to rest-frame powers eliminates calibration-dependent factors:

$$\frac{\bar{W}_{\text{lab}}(\theta_i)}{\bar{W}_{\text{rest}}(\theta_i)} = \frac{P_{E_y}(\theta_i, \beta_{\text{EB}})}{P_{E_y}(\theta_i, 0)} \frac{1}{D_i^2} \frac{\int \sigma(D_i\omega') d\omega'}{\int \sigma(\omega) d\omega}. \quad (\text{B16})$$

In the high-frequency limit where $\sigma(\omega) \approx \nu/\omega^2$, the integrals over the same frequency window are related by

$\int \sigma(D\omega') d\omega' \approx D^{-1} \int \sigma(\omega) d\omega$, and the ratio simplifies to

$$\frac{\bar{W}_{\text{lab}}}{\bar{W}_{\text{rest}}} \approx \frac{P_{E_y}(\theta_i, \beta)}{P_{E_y}(\theta_i, 0)} \frac{1}{D_i^2}. \quad (\text{B17})$$

Define the measured Doppler factor at pixel i :

$$D_i^{(\text{meas})} = \sqrt{\frac{P_{E_y}(\theta_i, \beta_{\text{EB}})}{P_{E_y}(\theta_i, 0)} \frac{\bar{W}_{\text{rest}}(\theta_i)}{\bar{W}_{\text{lab}}(\theta_i)}}. \quad (\text{B18})$$

The laboratory-frame temperature at each pixel is then

$$T_{\text{lab}}(\theta_i) = \frac{T_0}{D_i^{(\text{meas})}}, \quad (\text{B19})$$

and the recovered rest-frame temperature is

$$T_0^{(\text{rec})}(\theta_i) = T_{\text{lab}}(\theta_i) \times D_i, \quad (\text{B20})$$

where $D_i = \gamma_{\text{EB}}(1 - \beta_{\text{EB}} \cos \theta_i)$ uses the E - B velocity. Consistency of $T_0^{(\text{rec})}$ across all pixels verifies that the angular temperature profile has the form $T_0/D(\theta)$ predicted by the covariant FDT.

7. Noise injection model

Additive detector noise is modeled as a flat power floor at each pixel. For a given signal-to-noise ratio, the noise power per pixel is

$$P_{\text{noise}} = \frac{\langle \bar{W}_{\text{lab}} \rangle_{\theta}}{\text{SNR}}, \quad (\text{B21})$$

where $\langle \cdot \rangle_{\theta}$ denotes the average over pixels. Each noise trial draws an independent realization $\eta_i \sim \text{Exp}(1)$ (exponential with unit mean, appropriate for the chi-squared distribution of power in a single frequency bin with two degrees of freedom), and the noisy pixel power is

$$W_i^{(\text{noisy})} = \bar{W}_{\text{lab},i} + P_{\text{noise}} \eta_i. \quad (\text{B22})$$

Noise subtraction replaces $W_i^{(\text{noisy})}$ with $W_i^{(\text{noisy})} - P_{\text{noise}}$, removing the mean noise floor but leaving residual pixel-to-pixel scatter from the stochastic η_i .

8. Simulation parameters

Table II summarizes the parameters used for the HIGINS simulations.

The simulation code is publicly available at <https://github.com/IraWolfson/em-fluctuation-spectroscopy>.

TABLE II. Simulation parameters for the HIGGINS laser-plasma system.

Parameter	Symbol	Value
Electron density	n_e	10^{19} cm^{-3}
Plasma frequency	ω_p	$1.78 \times 10^{14} \text{ rad/s}$
Electron temperature	T_0	1 keV ($8512 \hbar\omega_p$)
Collision rate	ν/ω_p	0.05
Frequency range	$[\omega_{\min}, \omega_{\max}]$	$[0.1, 13.0] \omega_p$
Modes per realization	N_{mode}	4×10^4
Number of pixels	N_{pix}	12
Pixel angles	θ_i	15° to 165° (uniform)
Pixel half-width	$\Delta\theta/2$	1.72°
Detector distance	R	50 cm
Pixel size	d	3 cm

EM Fluctuation Spectroscopy: $T_{\text{lab}}(\theta)$ Extraction
10000 realizations, 40000 modes each | $\beta_{EB} = 0.74561 \pm 0.01662$

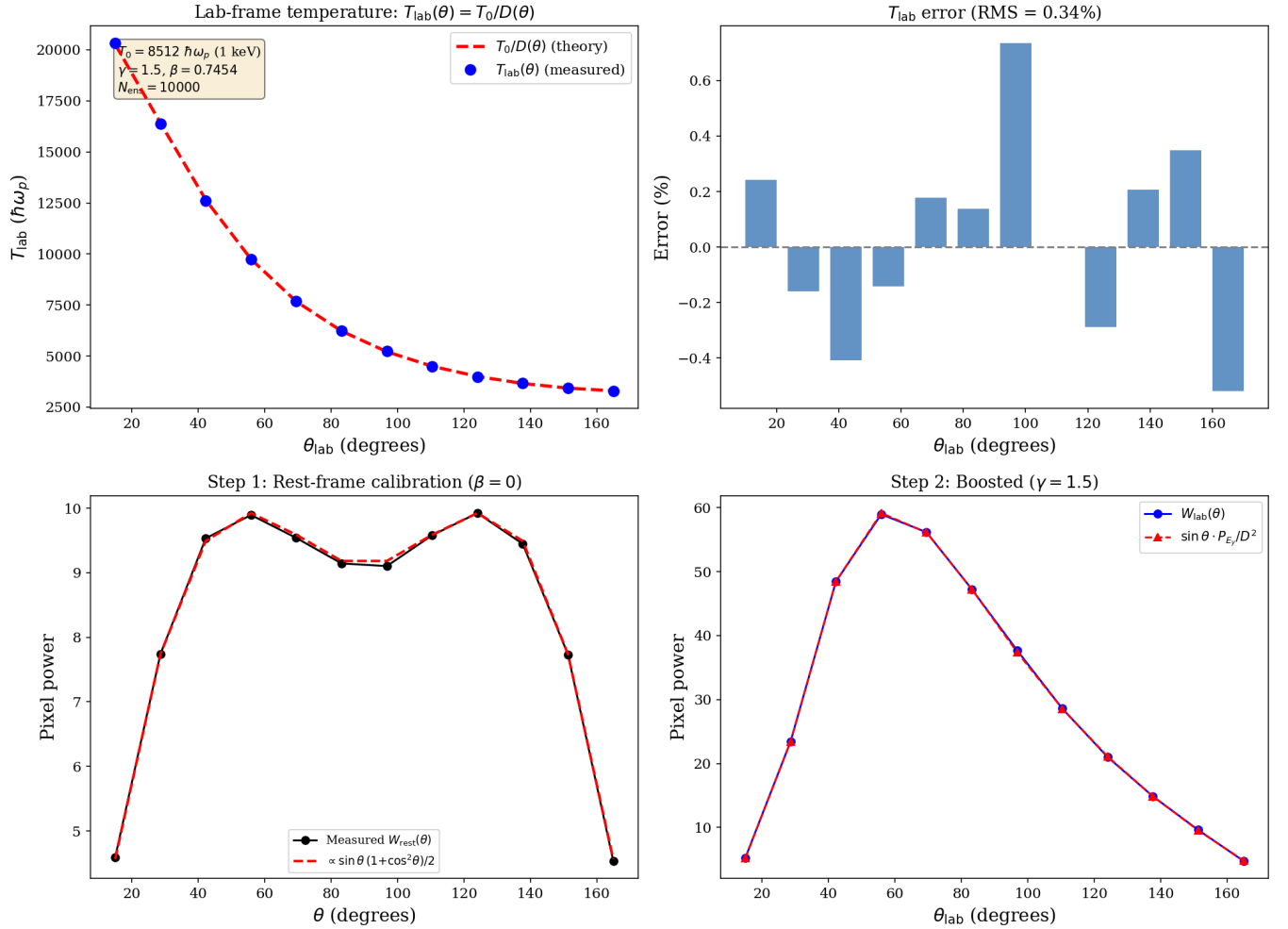


FIG. 1. Electromagnetic fluctuation spectroscopy at HIGGINS laser-plasma parameters ($T_0 = 8512 \hbar\omega_p = 1 \text{ keV}$, $\gamma = 1.5$, $\omega_p \approx 28 \text{ THz}$). 10^4 ensemble realizations with 4×10^4 modes each. Top left: Angular temperature profile $T_{\text{lab}}(\theta) = T_0/D(\theta)$ extracted from the two-step calibration protocol (blue points) compared with the theoretical prediction (dashed red line). Top right: Per-pixel extraction error; RMS = 0.34%. Bottom left: Rest-frame calibration: measured pixel power versus angle matches $\sin\theta(1+\cos^2\theta)/2$ angular dependence. Bottom right: Boosted-frame pixel power versus angle matches $\sin\theta P_{E_y}(\theta, \beta)/D^2(\theta)$.

Electromagnetic fluctuation spectroscopy: multi- γ validation
 $T_0 = 8512 \hbar\omega_p$ (1 keV), $N_{\text{cal}} = N_{\text{boost}} = 10^3$ realizations, 4×10^4 modes each

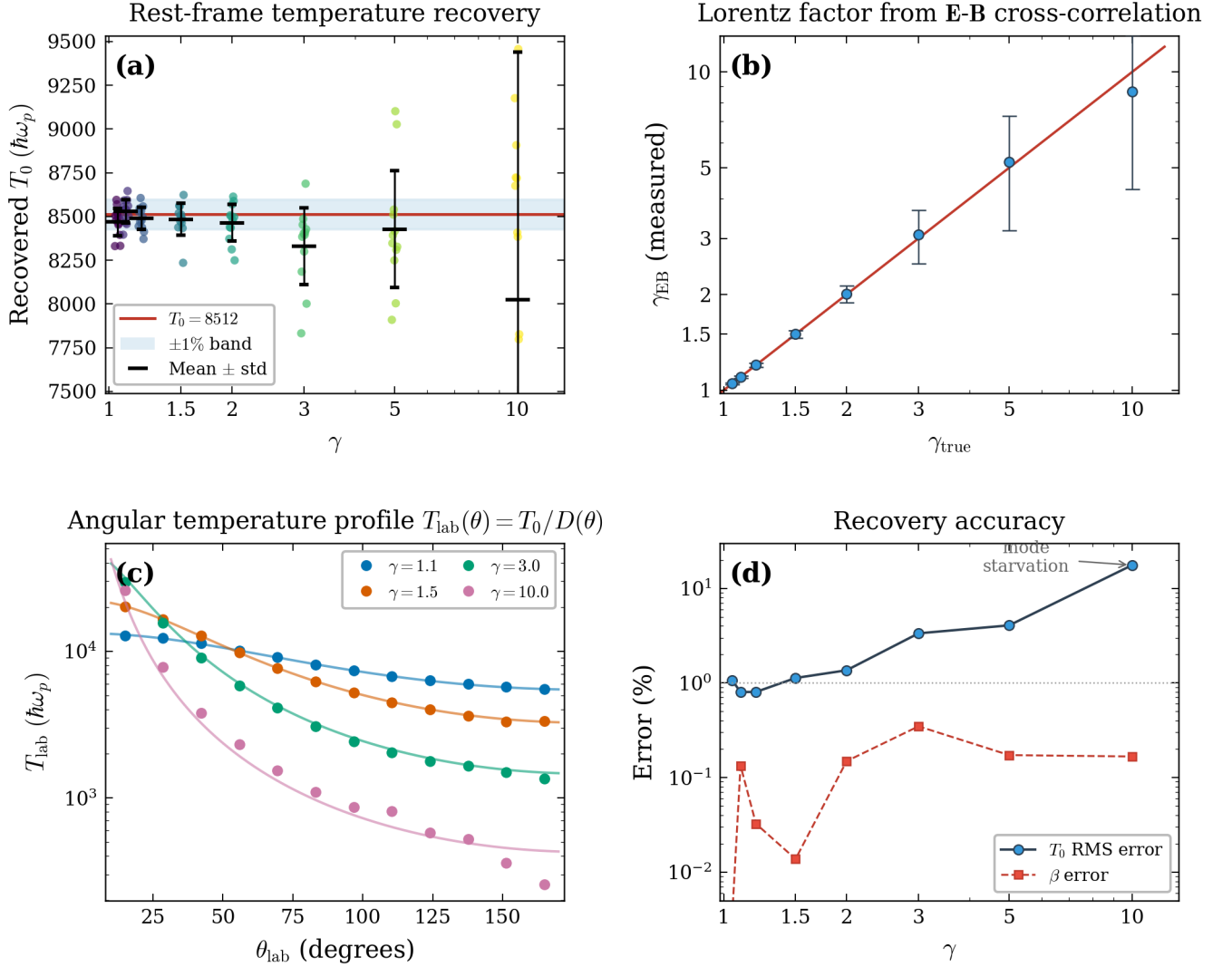


FIG. 2. Multi- γ validation of T_0 recovery. 10^3 calibration and 10^3 boosted realizations per γ , 4×10^4 modes each. (a) Recovered T_0 at each of 12 detector pixels for eight Lorentz factors; blue shading indicates $\pm 1\%$ band. Sub-percent recovery for $\gamma \leq 2$. (b) γ_{EB} from E - B cross-correlation versus true γ ; error bars from ensemble standard deviation. (c) Angular temperature profiles at selected γ ; solid lines: theory, points: measured. (d) RMS recovery error for T_0 (circles) and β (squares) versus γ . The increase above $\gamma \sim 3$ reflects mode starvation at backward angles due to relativistic beaming.

Noise susceptibility: additive detector noise on ensemble-averaged PSD
 $T_0 = 8512 \hbar\omega_p$, 1000 noise trials per SNR, $N_{\text{ens}} = 1000$ clean realizations

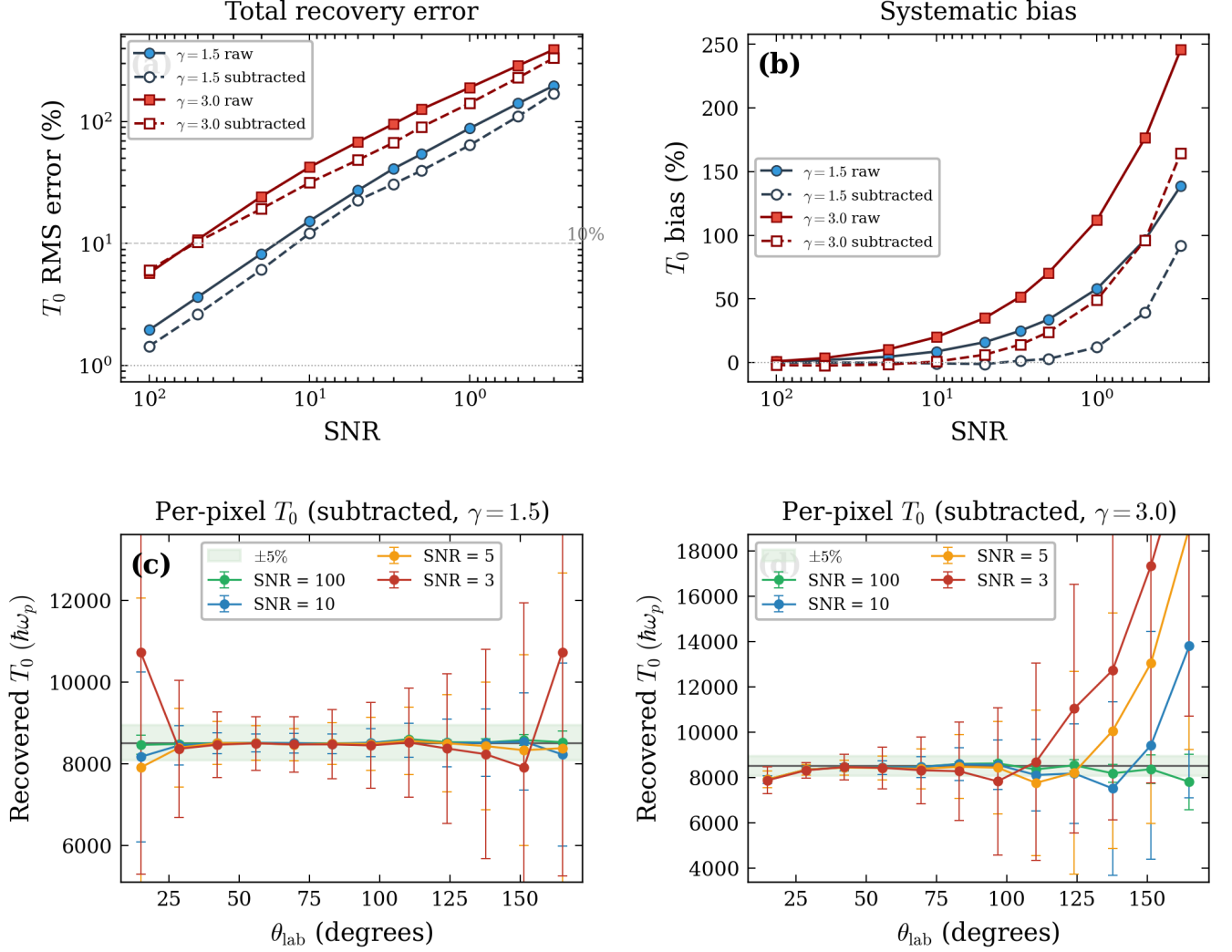


FIG. 3. Noise susceptibility analysis with additive detector noise. 10^3 clean realizations, 10^3 noise trials per SNR. (a) Total T_0 recovery error (RMS) versus SNR for $\gamma = 1.5$ (circles) and $\gamma = 3.0$ (squares); solid: raw, dashed: noise-subtracted. The 10% threshold is indicated. (b) Systematic bias in T_0 versus SNR: raw measurements are biased upward $\propto 1/\text{SNR}$; dark subtraction eliminates the bias. (c,d) Per-pixel T_0 recovery (noise-subtracted, mean \pm std over 10^3 trials) at selected SNR values for $\gamma = 1.5$ and $\gamma = 3.0$; green band indicates $\pm 5\%$.

Adversarial robustness tests: HIGGINS parameters ($\gamma = 1.5$, $T_0 = 1$ keV, $N_{\text{ens}} = 500$)

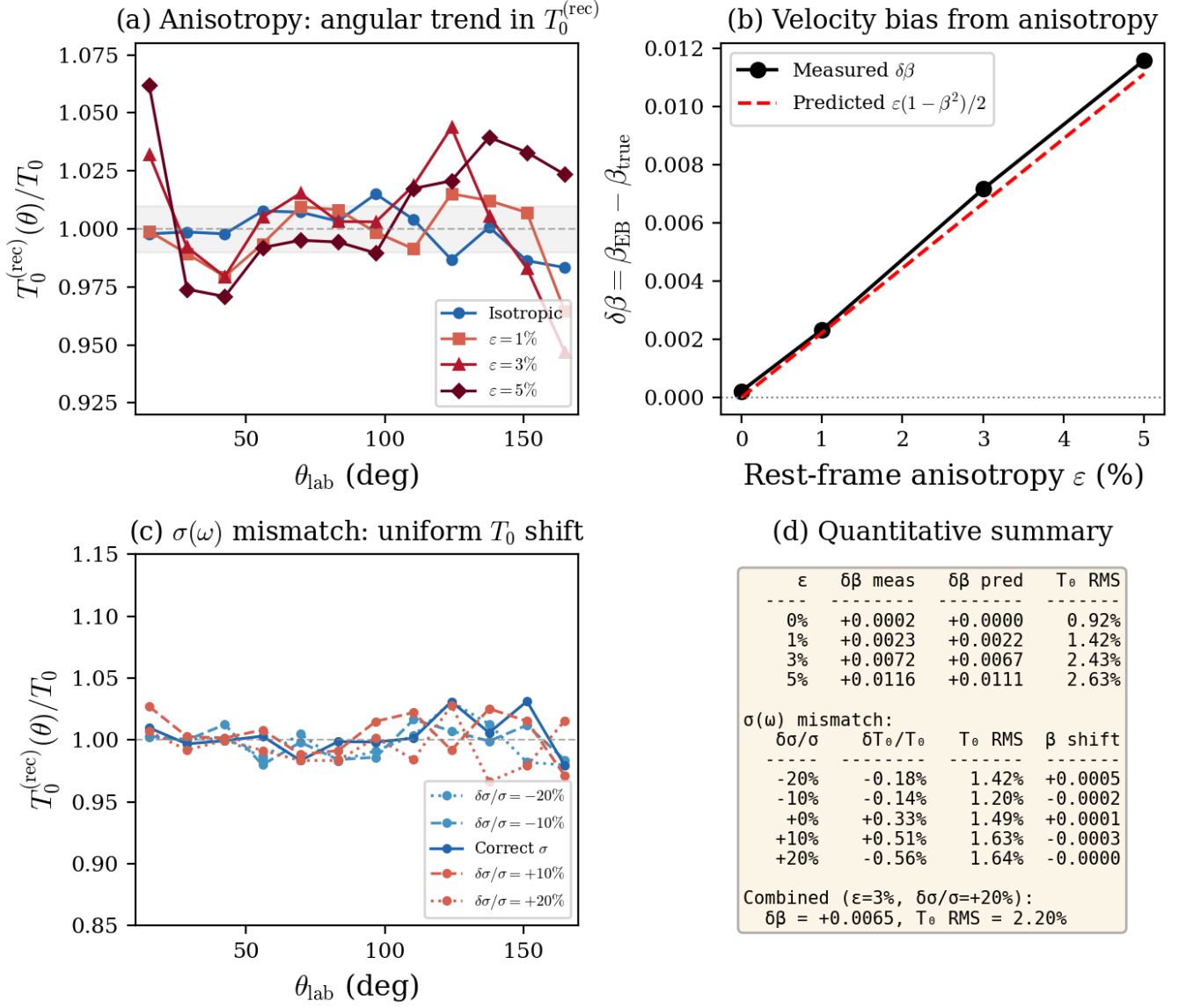


FIG. 4. Adversarial robustness tests at HIGGINS parameters ($\gamma = 1.5$, $T_0 = 1$ keV, $N_{\text{ens}} = 500$). (a) Recovered rest-frame temperature $T_0^{(\text{rec})}(\theta)/T_0$ versus laboratory angle for rest-frame anisotropy levels $\epsilon = 0$ (isotropic), 1%, 3%, and 5%; increasing anisotropy produces systematic angular trends in the recovered temperature profile. (b) Velocity bias $\delta\beta = \beta_{\text{EB}} - \beta_{\text{true}}$ versus anisotropy; black points: measured, dashed red: predicted $\epsilon(1 - \beta^2)/2$ from leading-order error propagation. (c) Same as (a) but for conductivity mismatches $\delta\sigma/\sigma = \pm 10\%$, $\pm 20\%$; the shift in T_0 is uniform across angles with no angular structure, and β_{EB} is unaffected. (d) Quantitative summary. The two failure modes—anisotropy and conductivity error—are experimentally distinguishable: the former introduces angular trends and biases β_{EB} , the latter shifts T_0 uniformly without affecting velocity recovery.